Research Article

Nano Research
2024, 17(6): 4872–4881

ISSN 1998-0124 CN 11-5974/O4
https://doi.org/10.1007/s12274-024-6474-z

Heterostructure Cu_3P-Ni_2P/CP catalyst assembled membrane electrode for high-efficiency electrocatalytic nitrate to ammonia

Meng Jin[1,2,§], Jiafang Liu[1,2,§], Xian Zhang[3] (✉), Shengbo Zhang[1,2], Wenyi Li[1,2], Dianding Sun[1,2], Yunxia Zhang[1,2], Guozhong Wang[1,2], and Haimin Zhang[1,2] (✉)

[1] *Laboratory of Materials Physics, Centre for Environmental and Energy Nanomaterials, Anhui Key Laboratory of Nanomaterials and Nanotechnology, CAS Center for Excellence in Nanoscience, Institute of Solid State Physics, Hefei Institutes of Physical Science, Chinese Academy of Sciences, Hefei 230031, China*
[2] *University of Science and Technology of China, Hefei 230026, China*
[3] *Anhui Contango New Energy Technology Co., Ltd., Hefei 230031, China*
[§] *Meng Jin and Jiafang Liu contributed equally to this work.*

© Tsinghua University Press 2024

Received: 16 November 2023 / **Revised:** 21 December 2023 / **Accepted:** 6 January 2024

ABSTRACT

Electrochemical nitrate reduction reaction (NO_3RR) is a promising means for generating the energy carrier ammonia. Herein, we report the synthesis of heterostructure copper-nickel phosphide electrocatalysts via a simple vapor-phase hydrothermal method. The resultant catalysts were evaluated for electrocatalytic nitrate reduction to ammonia (NH_3) in three-type electrochemical reactors. In detail, the regulation mechanism of the heterogeneous Cu_3P-Ni_2P/CP-*x* for NO_3RR performance was systematically studied through the H-type cell, rotating disk electrode setup, and membrane-electrode-assemblies (MEA) electrolyzer. As a result, the Cu_3P-Ni_2P/CP-0.5 displays the practicability in an MEA system with an anion exchange membrane, affording the largest ammonia yield rate (R_{NH3}) of 1.9 mmol·h^{-1}·cm^{-2}, exceeding most of the electrocatalytic nitrate reduction electrocatalysts reported to date. The theoretical calculations and *in-situ* spectroscopy characterizations uncover that the formed heterointerface in Cu_3P-Ni_2P/CP is beneficial for promoting nitrate adsorption, activation, and conversion to ammonia through the successive hydrodeoxygenation pathway.

KEYWORDS

electrocatalytic nitrate reduction to ammonia, three-type reactors, membrane-electrode-assemblies system, operando ATR-IRRAS, successive hydrodeoxygenation pathway

1 Introduction

Ammonia as an important feedstock chemical, plays a crucial role in the agriculture and pharmaceutical industry and shows great promise in becoming the next-generation energy carrier owing to its merits of high energy density (4.3 kWh·kg^{-1}) [1–3]. Currently, the Haber–Bosch process, employed for artificial nitrogen (N_2) fixation, necessitates elevated temperatures (> 450 °C) and high pressures (150–350 atm) [4–6]. This process releases a large amount of CO_2 to aggravate the greenhouse effect [7, 8]. Therefore, seeking clean, economical, and sustainable alternative ammonia synthesis methods has attracted much attention.

As we know, compared with the N≡N bond of N_2, the nitrate anion (NO_3^-) possesses a lower dissociation energy for breaking the N=O bond (204 kJ·mol^{-1}) [9–11]. Furthermore, NO_3^- is abundant in various sources such as industrial wastewater and agriculture production [12]. The United States Environmental Protection Agency (US EPA) and World Health Organization (WHO) declare that the concentration of NO_3^- in drinking water should be much lower than the 10.0 mg·L^{-1} as N-NO_3^-. Therefore, the process of converting nitrate to ammonia has the potential to solve the problem of environmental pollution and reduce energy consumption [13, 14]. Electrocatalytic nitrate reduction (NO_3RR), driven by renewable energy under ambient conditions, boasts superior reaction kinetics compared to electrocatalytic N_2 reduction reaction (NRR), thus gaining notable research attention [15]. However, the NO_3RR process still suffers from multiple difficulties, and is an intricate process involving multiple electrons and protons transfer, and numerous intermediates [16–21]. Additionally, the NO_3RR process is fiercely contested by hydrogen evolution reactions (HER) at high overpotentials, ultimately resulting in the low Faradaic efficiency (FE) [22, 23]. Consequently, it is imperative to design and develop high-efficiency NO_3RR electrocatalysts and electrocatalysis systems to produce ammonia.

Recently, the construction of heterostructure interfaces has gained recognition as a potent approach for manipulating a catalyst's electronic structure and active sites [24, 25]. These constructed heterointerfaces play a dual role, including the conservation of the catalytic activity of each active component and synergistically enhancing the catalytic performance attributed to the interfacial effect [26–31]. In this context, the transition metal phosphides have emerged as standouts due to their exceptional electrocatalytic activities and remarkable conductivity [32, 33]. For

Address correspondence to Xian Zhang, zhangxian158229@163.com; Haimin Zhang, zhanghm@issp.ac.cn

example, Pan et al. fabricated three-dimensional (3D) networked $Ni(OH)_2/Ni_3S_2$ hybrids via a hydrothermal method, and then Ni_2P/Ni_3S_2 hetero-nanoflake arrays were obtained through the phosphorization [34]. As an electrocatalyst, the obtained Ni_2P/Ni_3S_2 exhibited significantly enhanced electrochemical water splitting performance ascribed to strong interfacial coupling effects. Yu and co-workers fabricated the Ni–Mn–FeP nanoarrays through successive etching-depositing and phosphorization technology [35]. At a current density of 100 mA·cm^{-2}, the cell voltage was obtained to be only 1.55 V for overall water splitting due to the doping effect promoting the conversion of *O to *OOH and the adsorption processes of H*. Xu et al. fabricated the Cu/Pd/CuO_x heterostructures catalysts and achieved an excellent ammonia yield of 1510.3 μg·h^{-1}·mg$_{cat}^{-1}$ and the FE of 84.04% [36]. The density functional theory (DFT) calculations revealed that the Pd and Cu sites were the electron-deficient and electron-rich sites, respectively. NO_3^- was preferred to be adsorbed at Pd sites, and subsequently reduced at the Cu sites. Besides electrocatalysts, the electrochemical NO_3RR reactor is also critically important to obtain high-efficiency conversion of NO_3RR to NH_3. To date, almost all reported electrocatalytic NO_3RR works are exclusively using H-type electrochemical reactors [37], however, this approach also leads to lower utilization efficiency of electrocatalysts. Recently, Wang et al. reported the utilization of the membrane-electrode-assemblies (MEA) approach using a bipolar membrane with Co 3D nanoarray electrocatalyst for NO_3RR to NH_3, delivering an NH_3 yield rate of 68.4 mg·h^{-1}·cm^{-2} with a Faradaic efficiency of 86.2% at 1000 mA·cm^{-2} [38]. This inspired us to develop an innovative MEA system for high-efficiency electrocatalytic NO_3RR to NH_3.

Herein, we fabricated heterostructure copper-nickel phosphide electrocatalysts (Cu_3P-Ni_2P/CP-*x*, *x* represents the molar ratio of Cu_3P to Ni_2P) on carbon paper via a facile vapor-phase hydrothermal (VPH) method as we reported previously [39, 40]. As an electrocatalyst, the optimal Cu_3P-Ni_2P/CP-0.5 achieved an excellent ammonia yield rate (R_{NH3}) of 3.21 ± 0.44 mg·h^{-1}·cm^{-2} and a FE_{NH3} of 95.25% ± 2.83% in 0.5 M Na_2SO_4 at −0.6 V (vs. reversible hydrogen electrode (RHE)) in an H-type cell. Meanwhile, the rotating disk electrode (RDE) measurement results revealed that the increase of Ni_2P in the catalyst was beneficial for boosting the selectivity of ammonia production. Furthermore, we attempted to assemble the Cu_3P-Ni_2P/CP-0.5 into a MEA system, achieving an industrial-scale ammonia production performance (1.9 mmol·h^{-1}·cm^{-2}) at 2.6 V. Combining the spectroscopy characterizations and theoretical calculations, the results uncovered that the optimized electronic structure of Cu_3P and Ni_2P heterointerface would be very beneficial for enhancing the nitrate adsorption and activation, effectively inhibiting the competitive HER. This work would be helpful for the design and development of high-efficiency electrocatalysts and electrocatalysis systems for electrocatalytic nitrate to ammonia.

2 Experimental

2.1 Chemicals and materials

Sodium sulfate anhydrous, sodium nitrate, sodium nitrate-^{15}N ($Na^{15}NO_3$), ammonium sulfate, ammonium sulfate-$^{15}N_2$ ($(^{15}NH_4)_2SO_4$), deuterium oxide, $NiCl_2·6H_2O$, $CuCl_2·2H_2O$, sodium hydroxide (NaOH), sulfuric acid (H_2SO_4), and red phosphorus were purchased from Shanghai Sinopharm Chemical Regent Co., Ltd. Iridium black (Ir) and Fumion ionomer solutions (FAA-3-solut-10) were purchased from Anhui Contango New Energy Technology Co., Ltd. All chemicals were used without further treatment and purification. Anion-exchange membrane (AEM, FAA-3-50) was purchased from Suzhou Sinero Technology Co., Ltd. The commercial carbon paper (CP) was purchased from Shanghai Hesen Electric Co., Ltd. The resistivity of the used deionized water was 18.2 MΩ·cm.

2.2 Pre-treatment of CP

HNO_3 (65 wt.%) solution was used for CP pre-treatment (2.0 cm × 2.0 cm) to increase the surface functional groups (e.g., -OH, -COOH). Then, the CP was adequately washed with ethyl alcohol and deionized water at ambient conditions.

2.3 Fabrication of the Cu_3P/CP, Cu_3P-Ni_2P/CP-*x*, and Ni_2P/CP electrodes

The self-supported Cu_3P/CP, Cu_3P-Ni_2P/CP-*x*, and Ni_2P/CP were directly grown on the CP substrate via a facile VPH method (Fig. S1 in the Electronic Supplementary Material (ESM)) [39]. The pre-treated CP was first put into 6.0 mM Cu^{2+} or Ni^{2+} or the mixture of Cu^{2+} and Ni^{2+} aqueous solution for immersion of 24 h. After freeze-drying for 12 h, the Cu^{2+} or Ni^{2+} or Cu^{2+}/Ni^{2+} adsorbed CP was used as a precursor and placed on a Teflon holder (100 mL) containing 0.35 g of red phosphorus and 20 mL of 3.0 M NaOH solution for the VPH reaction. The VPH reaction was operated at 220 °C for 0.5 h. The obtained samples were denoted as Cu_3P/CP, Ni_2P/CP, and Cu_3P-Ni_2P/CP-*x*.

2.4 Electrochemical measurements

The electrochemical measurements were performed on the electrochemical workstation (CHI 760D) in an H-type electrolytic cell (separated by an FAA-3-50 anion-exchange membrane) in 0.5 M Na_2SO_4. In this three-electrode system, Pt mesh and Ag/AgCl (saturated KCl) were used as the counter electrode and reference electrode, while the *in-situ* grown Cu_3P/CP, Cu_3P-Ni_2P/CP-*x*, and Ni_2P/CP self-supported electrodes were used as the working electrodes. Ammonia synthesis was carried out in a 0.5 M Na_2SO_4 solution (50 mL) of 200 ppm $NaNO_3$-N saturated with Ar, and the potentiostatic test was performed for 2 h. For the linear sweep voltammetry (LSV) tests, the polarization curves were obtained at a scanning rate of 5.0 mV·s^{-1} from −0.21 to −1.61 V. The potentiostatic test was performed in 0.5 M Na_2SO_4 at different potentials. The potentials in this work were converted to a RHE scale according to the following Eq. (1)

$$E_{RHE} = E_{Ag/AgCl} + 0.059pH + 0.197\ (V) \quad (1)$$

where *E* represents the potential, and V is the potential unit.

2.5 RDE measurements

The linear polarization curves were carried out in a rotating disk electrode (Pine MSR rotator). The catalysts stripped from the CP were deposited on a glassy carbon electrode (GCE, 0.247 cm^2) as the working electrode. The counter and reference electrodes were a platinum wire and an Ag/AgCl electrode, respectively. The catalyst ink was fabricated as follows: 5 mg powder was suspended in the mixture of 20 μL distilled water, 940 μL ethanol, and 40 μL of 5 wt.% Nafion solution, followed by sonicating for 30 min. Then 10 μL catalyst ink was dropwise cast on the glass carbon electrode and dried up at 40 °C for 10 min. For the NO_3RR experiments, the 0.5 M Na_2SO_4 electrolyte (contained 200 ppm $NaNO_3$-N) was continuously bubbled with Ar for at least 30 min, and then the Ar flow rate was decreased to 15 mL·min^{-1} during the NO_3RR experiments The number of exchanged electrons (*n*) was calculated as the Koutécky–Levich (K–L) equations (Eqs. (2) and (3))

$$1/j = 1/j_k + 1/j_d = 1/j_k + 1/(B\omega^{1/2}) \quad (2)$$

$$B = 0.62nFC_0D_0^{2/3}\nu^{-1/6} \quad (3)$$

where j_k is kinetic current density, j_d is diffusion-limited current density, ω represents the electrode's rotation rate (rpm), n is the number of exchanged electrons, F is the Faraday constant (96,485 C·mol^{-1}), C_0 is the nitrate concentration, ν is the kinematic viscosity of the electrolyte, and D_0 is the diffusion coefficient [41–43].

2.6 Preparation of working electrode for MEA measurement

The electrochemical NO_3RR measurements were carried out in a commercial MEA electrolyzer purchased from Anhui Contango New Energy Technology Co., Ltd. The preparation of anode catalyst ink was as follows: 15 mg Ir powder was suspended in the mixture solution of 1.0 g deionized water, 4.0 g of isopropyl alcohol, and 0.22 g FAA-3-solut-10 ionomer solution. The anode catalyst ink was then spray-coated onto one side of anion exchange membrane as the anode catalyst layer and the area of the working electrode was 4.0 cm^2.

2.7 Electrocatalytic NO_3RR in MEA system

The MEA electrolyzer was constituted with a titanium flow field for the anode side, while the graphite plate was for the cathode side. The MEA electrolyzer consisted of the Cu_3P-Ni_2P/CP-0.5 (4.0 cm^2) as the cathode and the Ir was used as the anode catalyst. On the anodic side, the flow channel was supplied with 1.0 M NaOH solution, while the cathodic side was circulated with 200 ppm $NaNO_3$-N solution. Different cell voltages were applied ranging from 1.6 to 2.8 V to evaluate the electrocatalytic NO_3RR performance in the MEA reactor.

2.8 Theoretical calculations

All the first-principle calculations were performed by using the Vienna *ab initio* simulation package (VASP) [40]. The inert core electrons were described through the projector augmented wave (PAW) method [44]. The electronic exchange-correlation effects were described with Perdew–Burke–Ernzerhof generalized gradient approximation (PBE-GGA) functional [45]. The long range van der Waals interaction was described by the empirical correction (DFT+D3) [46, 47]. A cutoff energy of 400 eV was used. The total energy changed within 10^{-5} eV·atom^{-1} and the Hellmann–Feynman force was less than 0.02 eV·Å^{-1}. The $p(2 \times 2)$ supercell of Cu_3P, Ni_2P, and Cu_3P-Ni_2P with the 6-layer surface of the $p(2 \times 2)$ slab model was constructed and 3 layers were fixed. The z-direction vacuum was 15 Å. The VASPKIT code was used for the post-processing of the DFT calculated data [48].

The change of the Gibbs free energy can be calculated as Eq. (4)

$$\Delta G = \Delta E + \Delta \mathrm{ZPE} - T\Delta S \quad (4)$$

In order to avoid directly calculating the energy of NO_3^-, gaseous HNO_3 was taken as a reference, and the steps are as follows ((Eqs. (5)–(7)) [49]

$$\mathrm{HNO_3(g)} \rightarrow \mathrm{HNO_3(l)} \quad (5)$$

$$\mathrm{HNO_3(l)} \rightarrow \mathrm{H^+ + NO_3^-} \quad (6)$$

$$* + \mathrm{NO_3^-} \rightarrow *\mathrm{NO_3} + \mathrm{e^-} \quad (7)$$

The adsorption of NO_3^- can be described as follows (Eq. (8))

$$* + \mathrm{HNO_3} \rightarrow *\mathrm{NO_3} + \mathrm{H^+} + \mathrm{e^-} \quad (8)$$

Herein, the adsorption energy of NO_3^- can be calculated as Eqs. (9) and (10)

$$\Delta G_{*\mathrm{NO_3}} = G_{*\mathrm{NO_3}} - G_* - G_{\mathrm{HNO_3(g)}} + 0.5{*}G_{\mathrm{H_2(g)}} + \Delta G_{\mathrm{correct}} \quad (9)$$

$$\Delta G_{\mathrm{correct}} = -\Delta G_5 - \Delta G_6 \quad (10)$$

2.9 Operando attenuated total reflection surface-enhanced infrared adsorption spectroscopy (ATR-IRRAS)

The operando attenuated total reflection surface-enhanced infrared adsorption spectroscopy measurements were performed on the Thermo Fisher iS50 FTIR equipment. The resolution of the sample spectra was 64 cm^{-1}. The potential region was from −0.2 to −1.0 V (vs. RHE). The *in-situ* ATR-IRRAS setup is shown in Fig. S22 in the ESM.

3 Results and discussion

3.1 Structure and morphology of Cu_3P-Ni_2P/CP-x

In this work, a series of bimetallic copper-nickel phosphide electrocatalysts grown on commercial carbon paper (denoted as Cu_3P-Ni_2P/CP-x, x represents the molar ratio of Cu_3P to Ni_2P) were synthesized via a facile VPH method (Fig. 1(a) and Fig. S1 in the ESM) [39]. For a meaningful comparison, individual copper phosphide (Cu_3P/CP) and nickel phosphide (Ni_2P/CP) grown on CP were also fabricated using the same method. The X-ray diffraction (XRD) patterns of Cu_3P/CP and Ni_2P/CP showed that the diffraction peaks at 36.0°, 39.1°, 41.2°, 45.1°, 46.1°, and 47.3° can be assigned to the hexagonal Cu_3P (JCPDS No. 02-1263), while the other diffraction peaks at 40.8°, 44.6°, 47.3°, 54.2°, and 54.9° agree well with the hexagonal Ni_2P (JCPDS No. 03-0953) (Fig. 1(b)). For Cu_3P-Ni_2P/CP-0.5 and Cu_3P-Ni_2P/CP-2 samples, the diffraction peaks belonging to Cu_3P and Ni_2P can also be obviously observed, indicating co-presence of Cu_3P and Ni_2P in these two samples. The morphological characterizations of Cu_3P-Ni_2P/CP-0.5 and Cu_3P-Ni_2P/CP-2 were confirmed by the scanning electron microscope (SEM) (Figs. 1(c) and 1(d), and Fig. S2 in the ESM). As shown, all copper-nickel phosphides are tightly attached to the carbon paper. Ni_2P/CP presented granular nanocrystals with interconnected porous structures on CP (Fig. S2(a) in the ESM), and the Cu_3P/CP showed a nanosheet structure (Fig. S2(b) in the ESM).

Unlike Ni_2P/CP and Cu_3P/CP, the surface morphology of Cu_3P-Ni_2P/CP-x was greatly affected by the molar ratio of Ni^{2+} to Cu^{2+} in the precursor. When Ni^{2+} content was lower than that of Cu^{2+}, the Cu_3P-Ni_2P/CP-2 mainly displayed the nanosheet structure (Fig. S2(c) in the ESM). Cu_3P was considered as the dominant component, and Ni_2P was believed to be the modification component [34]. With increasing Ni_2P content, the nanoparticles gradually increased, and finally presented the granular nanocrystals (Figs. 1(c) and 1(d)), in which the particle size of the Cu_3P-Ni_2P/CP-0.5 obviously increased as compared to Ni_2P/CP. The Cu_3P-Ni_2P/CP-x could establish rich heterointerfaces, which boosted the electron transfer, beneficial for electrocatalytic NO_3RR [50].

The transition electron microscopy (TEM) and high-resolution transition electron microscopy (HRTEM) images (Figs. 1(e) and 1(f), and Fig. S3 in the ESM) of Cu_3P-Ni_2P-0.5 showed the lattice spacings of 0.22 nm, which can be attributed to the Ni_2P (111) facet, and the lattice fringe spacing of 0.25 nm corresponded to the (-1-12) lattice plane of Cu_3P. Besides, the phase boundary between Cu_3P and Ni_2P on CP noted by the dashed line was clearly observed, confirming the formation of a heterointerface [34]. The

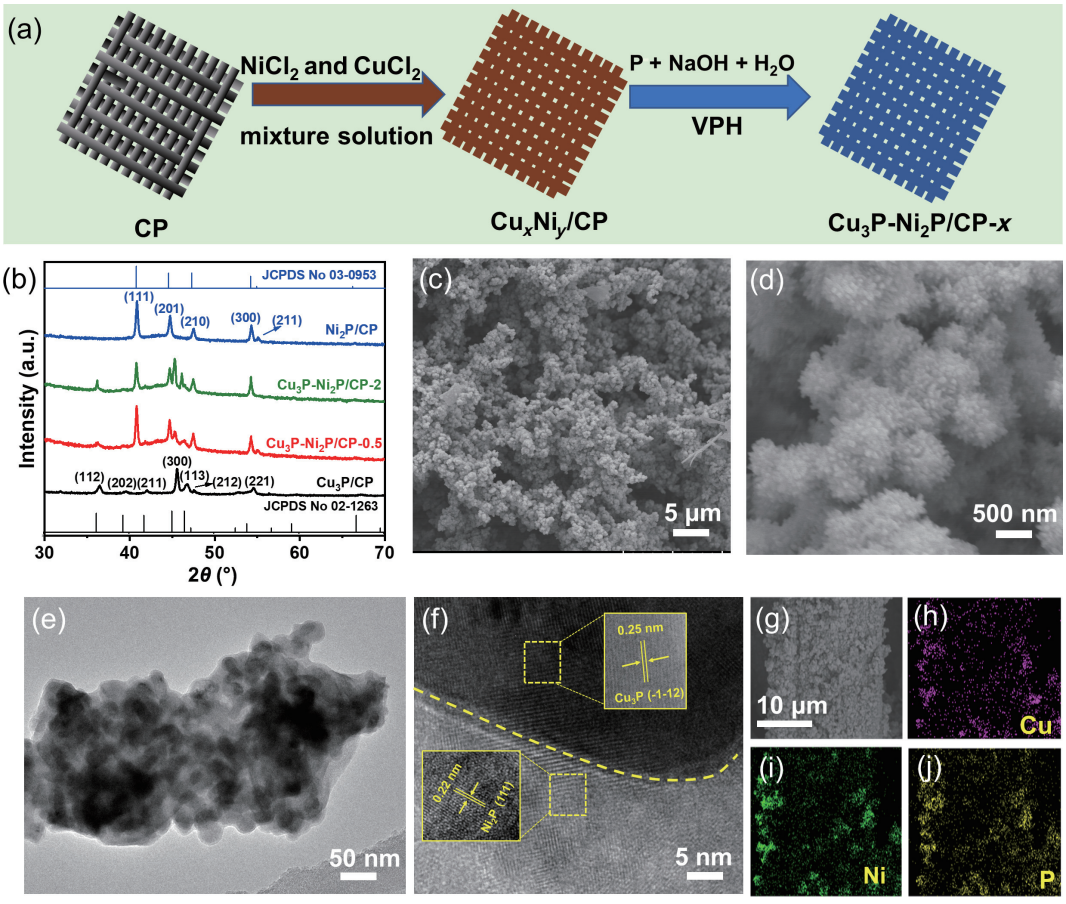

Figure 1 (a) Schematic illustration for Cu_3P-Ni_2P/CP-*x* catalysts fabrication process. (b) XRD patterns of the as-prepared Ni_2P/CP, Cu_3P-Ni_2P/CP-2, Cu_3P-Ni_2P/CP-0.5, and Cu_3P/CP. (c) Low-resolution and (d) high-resolution SEM images of Cu_3P-Ni_2P/CP-0.5. (e) TEM image and (f) HRTEM image of Cu_3P-Ni_2P/CP-0.5. (g)–(j) SEM image and the corresponding element mappings of Cu_3P-Ni_2P/CP-0.5.

composition of Cu_3P-Ni_2P/CP-0.5 was analyzed via the energy-dispersive X-ray (EDX) spectra mapping images (Figs. 1(g)–1(j)). It can be clearly seen that Cu, Ni, and P elements were uniformly distributed on the surface of carbon paper. The abovementioned results demonstrated the formation of Cu_3P-Ni_2P/CP-0.5 supported on carbon paper with the existence of a heterointerface. The chemical valences and electronic interactions of the obtained samples were analyzed via the X-ray photoelectron spectroscopy (XPS) technique. In the surface survey XPS spectra, the Ni, Cu, P, O, and C elements were present (Fig. 2(a)). For Ni_2P/CP sample (Fig. 2(b) and Fig. S4 in the ESM), the main peak of Ni 2p can be decomposed into two peaks at 853.7 and 871.3 eV, corresponding to the Ni–P species in Ni_2P [50]. The peaks at 856.8 and 874.1 eV as well as two satellite peaks (877.8 and 859.7 eV) can be indexed to Ni $2p_{3/2}$ and Ni $2p_{1/2}$ of nickel oxides species due to the surface oxidation of Ni_2P in air [39, 51]. Comparatively, the negative shift upon Ni 2p peak positions of Cu_3P-Ni_2P/CP-0.5 sample to lower binding energies happened, meaning that the nickel in Cu_3P-Ni_2P/CP-0.5 was readily accessed to electrons (Fig. 2(b)).

Figure 2(c) showed the Cu 2p XPS spectra of Cu_3P/CP and Cu_3P-Ni_2P/CP-0.5. The peaks of Cu_3P-Ni_2P/CP-0.5 at 934.5 (Cu $2p_{3/2}$), 936.7 (Cu $2p_{3/2}$), and 954.2 eV (Cu $2p_{1/2}$) with two satellite peaks at 943.6 and 963.2 eV were assigned to the oxidized Cu^{2+} [52, 53]. These peaks slightly shifted toward higher binding energy, indicating that the electrons are readily lost from copper in Cu_3P-Ni_2P/CP-0.5. The above high-resolution XPS spectra of Ni 2p and Cu 2p further confirmed the formation of heterointerfaces in Cu_3P-Ni_2P/CP-0.5, beneficial for electron transfer from Ni_2P to Cu_3P. In the P 2p XPS spectra of Cu_3P/CP, Ni_2P/CP, and Cu_3P-Ni_2P/CP-0.5, the peaks at 130.7, 131.9, and 133.8 eV were ascribed to the P $2p_{3/2}$, P $2p_{1/2}$, and oxidized P species [39, 54]. However, a negative shift of P 2p peaks was observed in Cu_3P-Ni_2P/CP-0.5 compared to Ni_2P/CP, and the P 2p XPS peaks of Cu_3P/CP also shifted toward lower binding energy compared to Cu_3P-Ni_2P/CP-0.5, implying the formation of heterointerfaces between Ni_2P and Cu_3P (Fig. 2(d)).

3.2 Electrochemical measurements

The electrocatalytic activities of these samples for NO_3RR were performed in 0.5 M Na_2SO_4 solution with a typical two-compartment three-electrode H-type cell in the Ar-saturated atmosphere. The corresponding products were detected using colorimetric methods and the calibration curves were presented in Fig. S5 in the ESM. LSV measurement was performed to study the catalyst's electrocatalytic performance with and without 200 $\mu g \cdot mL^{-1}$ NO_3^--N (Fig. S6 in the ESM). After the addition of NO_3^-, all electrocatalysts exhibited NO_3RR activity. Besides, the chronoamperometry technology was also used for investigating the nitrate electroreduction efficiency (Fig. S7 in the ESM). The faradaic efficiency presented a volcano-shaped curve, among which the Cu_3P-Ni_2P-0.5 possessed an excellent electrocatalytic activity for NO_3RR, delivering the maximum R_{NH3} of 4.54 ± 0.17 $mg \cdot h^{-1} \cdot cm^{-2}$ at −1.0 V (vs. RHE) and an optimal FE of 95.25% ± 2.83% for NH_3 production at −0.6 V (vs. RHE) (Fig. 3(a)).

At −0.6 V (vs. RHE), the Cu_3P-Ni_2P/CP-0.5 exhibited a R_{NH3} of 3.21 ± 0.44 $mg \cdot h^{-1} \cdot cm^{-2}$ with a FE of 95.25% ± 2.83%, which were higher than those of Cu_3P-Ni_2P/CP-2 (R_{NH3} of 2.29 ± 0.34 $mg \cdot h^{-1} \cdot cm^{-2}$, FE_{NH3} of 91.97% ± 1.66%), Cu_3P/CP (R_{NH3} of 1.81 ± 0.12 $mg \cdot h^{-1} \cdot cm^{-2}$, FE_{NH3} of 61.80% ± 1.45%), and Ni_2P/CP (R_{NH3} of 0.86 ± 0.06 $mg \cdot h^{-1} \cdot cm^{-2}$, FE_{NH3} of 45.14% ± 3.23%) (Fig. 3(b) and Figs. S8–S10 in the ESM). Additionally, no hydrazine by-product was detected for Cu_3P-Ni_2P/CP-0.5 during electrocatalytic NO_3RR

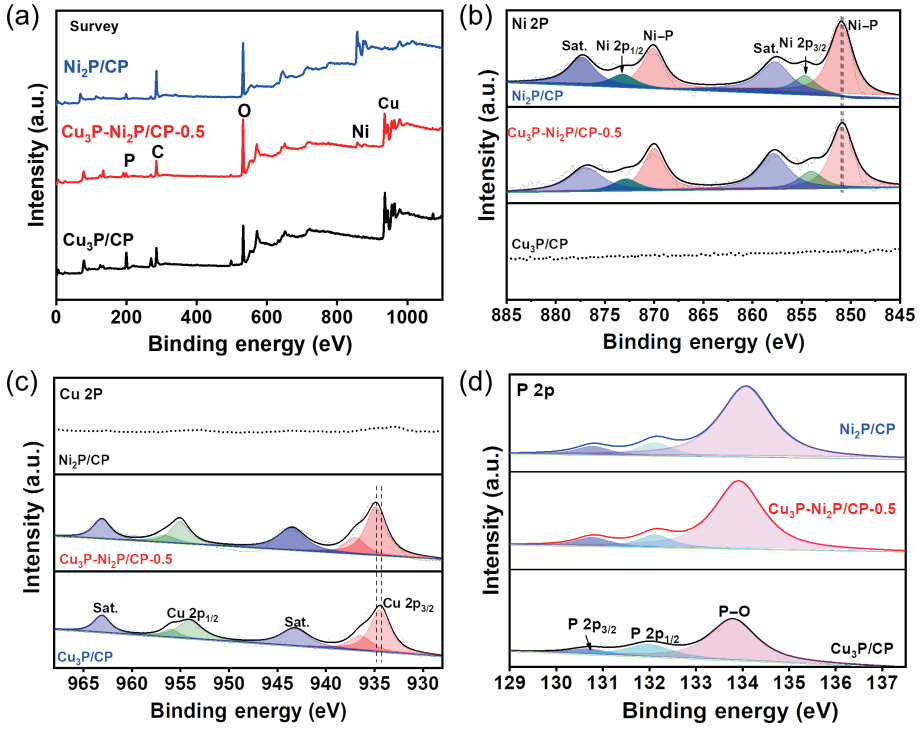

Figure 2 (a) The XPS spectra of Cu_3P/CP, Cu_3P-Ni_2P/CP-0.5, and Ni_2P/CP. The high-resolution spectra of (b) Ni 2p, (c) Cu 2p, and (d) P 2p.

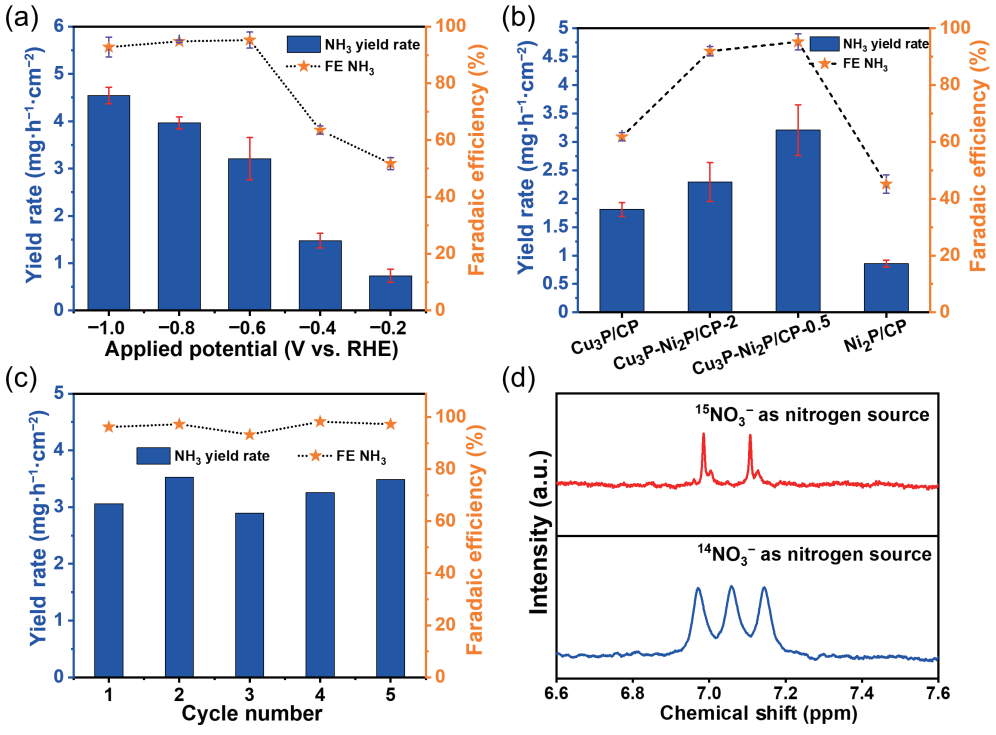

Figure 3 (a) Ammonia yield rate and FE at different potentials of Cu_3P-Ni_2P/CP-0.5 in 0.5 M Na_2SO_4 electrolyte with 200 μg·mL^{-1} NO_3^--N. (b) Ammonia yield rate and FE at −0.6 V (vs. RHE) potentials of Cu_3P/CP, Cu_3P-Ni_2P/CP-2, Cu_3P-Ni_2P/CP-0.5, and Ni_2P/CP in 0.5 M Na_2SO_4 electrolyte with 200 μg·mL^{-1} NO_3^--N. (c) Recycling stability test of Cu_3P-Ni_2P/CP-0.5 at −0.6 V (vs. RHE). (d) ^{1}H NMR spectra of Cu_3P-Ni_2P/CP-0.5 at −0.6 V (vs. RHE).

(Fig. S11 in the ESM). The electrocatalytic NO_3RR performance using Cu_3P-Ni_2P/CP-0.5 surpassed most of recently reported metal phosphide-based electrocatalysts in literatures (Table S1 in the ESM). The stability of the electrocatalysts was evaluated by cycling tests. After five cycles, the Cu_3P-Ni_2P/CP-0.5 still maintained high ammonia synthesis yield and Faradaic efficiency at −0.6 V (V vs. RHE) (Fig. 3(c)). In addition, the Cu_3P-Ni_2P/CP-0.5 maintained a slight decreased current density during 10 h of test period (Fig. S12 in the ESM), indicating high activity and stability of Cu_3P-Ni_2P/CP-0.5 toward electrocatalytic NO_3RR. To exclude the environmental interferences to NH_3 synthesis, a series of control experiments and isotopic labeling experiments were conducted in this work. As shown in Fig. S13 in the ESM, only ignorable ammonia was detected in an Ar-saturated 0.5 M Na_2SO_4 electrolyte under open circuit voltage (OCV) for 24 h. Furthermore, the ^{1}H nuclear magnetic resonance (NMR) spectra of electrolytes using $^{14}NO_3^-$-N and $^{15}NO_3^-$-N as the reactants were further carried out. The ^{1}H NMR of ^{15}N-NH_4^+ presented double peaks at δ = 6.99 and δ = 7.11 ppm, further verifying the ammonia product originated from the nitrate reduction process (Fig. 3(d)) [55].

3.3 The kinetics of electrocatalytic NO_3RR and MEA measurements

In this study, the as-obtained electrocatalysts were further tested on the RDE in 0.5 M Na_2SO_4 solution with or without NO_3^--N at a rotation rate of 1225 rpm to investigate the kinetics of electrocatalytic NO_3RR. Apparently, the Cu_3P-Ni_2P-0.5 showed the highest activity among all investigated electrocatalysts (Fig. S14 in the ESM). On the Ni_2P catalyst, a more negative cathodic potential was needed to achieve the same NO_3^--transport-limited current as Cu_3P-Ni_2P-0.5 (Fig. S14 in the ESM). Surprisingly, the plateau of the Cu_3P and Cu_3P-Ni_2P-2 was well obvious, indicating that this was an evident multi-electron transfer compared with the Cu_3P-Ni_2P-0.5 and Ni_2P (Fig. S14 in the ESM). Furthermore, RDE experiments with rotating rates varying from 400 to 1600 rpm were carried out (Fig. 4(a), and Figs. S15(a), S16(a), and S17(a) in the ESM) and the catalytic kinetics parameters were analyzed with the K–L curves (Fig. 4(b), and Figs. S15(b), S16(b), and S17(b) in the ESM). Typically, the cathodic current densities obviously increased accompanied by the increased speed, demonstrating the shortened diffusion distance at high rotation speeds [56]. The ammonia production selectivity of the electrocatalyst was further analyzed by estimating the average number of exchanged electrons (n) [57]. The slopes of the Cu_3P-Ni_2P-0.5 and Ni_2P corresponding K–L plots with good linearity were similar in the potential range from −0.3 to −0.8 V vs. RHE, indicating the number of transferred electrons was similar and remained constant at different potentials (Fig. 4(c) and Fig. S17(c) in the ESM) [57]. In detail, the n values of the Cu_3P-Ni_2P-0.5 and Ni_2P were calculated to be 7.71 and 7.39, proving that the 8-electron reduction process was taken place. For the referred Cu_3P and Cu_3P-Ni_2P-2, other by-products were formed except for the ammonia evidenced by the decreased n values (Figs. S15(c) and S16(c) in the ESM). Surprisingly, the regularity between the n values and the potential was similar to the FE_{NH3} observed in the H-type cell. Besides, the n value of Cu_3P-Ni_2P-0.5 was achieved at the maximum at −0.6 V (vs. RHE). For Ni_2P, Cu_3P, and Cu_3P-Ni_2P-2 catalysts, the peak of n values was achieved at −0.8 V (vs. RHE), corresponding to the maximum FE_{NH3} in the H-type cell (Fig. 3(a) and Figs. S8–S10 in the ESM).

In addition to catalyst design, the rational design of the electrochemical reactors is also of great significance for enhancing the performance of NO_3RR and realizing the large-scale application of NO_3RR [58]. In an H-type cell, since the reference electrode is closer to the working electrode, the applied potential can be precisely controlled, which is beneficial for fundamental studies [59]. However, huge ohmic resistance and low current density limit its industrial applications [58]. It is urgent to reduce the ohmic resistance of the H-type electrolytic cell. Compared with the H-type cell, the MEA system removes the aqueous electrolyte between the cathode and anode. In addition, the ion-conducting polymer (ionomer) serves as both the separator and electrolyte, ensuring the catalyst stability [60]. All of these can reduce the cell ohmic overpotential by increasing the electrolyte conductivity and reducing the distance between the two electrodes and improving energy efficiency [61]. MEA device was further used to evaluate the large-scale application of NO_3RR of the Cu_3P-Ni_2P-0.5 [58, 62]. The Cu_3P-Ni_2P/CP-0.5 was assembled to the MEA electrolyzer as the gas-diffusion electrode and pressed onto one side of the membrane, which promotes the transfer and distribution of reactants, achieving higher current density and lower transport losses (Fig. 4(h)) [62]. The current–voltage response vs. different temperatures was first tested in the MEA electrolyzer and the cyclic voltammogram curves were presented

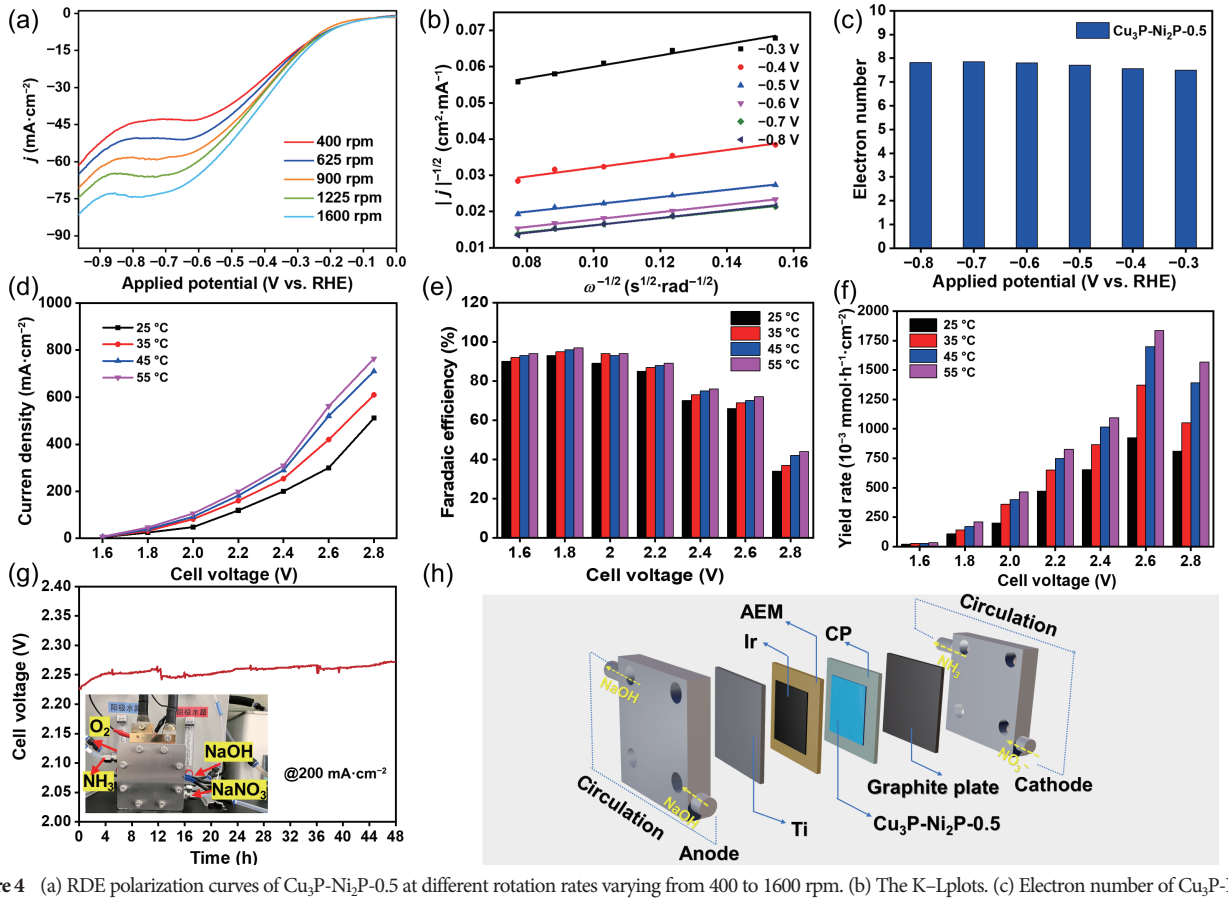

Figure 4 (a) RDE polarization curves of Cu_3P-Ni_2P-0.5 at different rotation rates varying from 400 to 1600 rpm. (b) The K–Lplots. (c) Electron number of Cu_3P-Ni_2P-0.5 at different applied potentials. (d) Relationship between current density and applied full-cell voltage for the electrolyzer with different temperatures. The corresponding (e) FEs and (f) yield rate of ammonia. (g) Voltage stability for a prolonged experiment run at 200 mA·cm^{-2}. (h) Schematic of MEA electrolyzer for NO_3RR process.

in Fig. 4(d). The current density exceeds the industrial current densities (200 mA·cm^{-2}) at the full-cell voltage of 2.2 V (55 °C), which is mainly ascribed to the increased membrane conductivity and the accelerated reaction kinetics of NO_3RR (Fig. 4(d)) [63, 64].

However, at the full-cell voltage of 2.8 V, the current density changes not significantly at a temperature above 45 °C. With the increased temperature, the FE of ammonia synthesis was slowed down, primarily due to the simultaneously happened HER process (Fig. 4(e)). Accordingly, the current density can reach 764 mA·cm^{-2} at the full-cell voltage of 2.8 V (55 °C) in the MEA system. Meanwhile, the FE was observed as a volcano-shaped curve similar to the H-type cell and the maximum of R_{NH3} was calculated to be 1.9 mmol·h^{-1}·cm^{-2} at a full cell voltage of 2.6 V (Fig. 4(f)). The voltage evolution of the electrocatalyst catalyst during 48 h constant current at 200 mA·cm^{-2} was presented in Fig. 4(g). The slightly degradation rate of cell voltage showed that the electrocatalyst material is applicable in the realistic industry.

3.4 Proposed reaction mechanism

To illustrate the relationship between the heterointerfaces and electrocatalytic activities of the fabricated catalysts, the DFT calculations were used to get the deep insight into the trends in reactivity and selectivity. The Ni_2P (001)-Cu_3P (1-10) surface was constructed as the optimized model of Cu_3P-Ni_2P-0.5 heterostructure (Figs. S18 and S19(a) in the ESM). The theoretical slab models of Cu_3P (1-10) and Ni_2P (001) were investigated as well for comparison (Figs. S19(b) and S19(c) in the ESM). It is generally accepted that NO_3^- adsorption is the first step for the electroreduction of NO_3RR [65]. The optimized models for NO_3^- adsorption on the Cu_3P (1-10), Ni_2P (001), and Ni_2P (001)-Cu_3P (1-10) surfaces are shown in Figs. 5(a) and 5(b). The NO_3^- (ΔG_{*NO3}) adsorption free energy values on Cu_3P (1-10) and Ni_2P (001) are 0.055 and 0.27 eV, respectively, indicating that the NO_3^- adsorption on these two surfaces is a uphill with energy consumption (Fig. 5(c)). As for Cu_3P-Ni_2P-0.5, the ΔG_{*NO3} moved negatively (−5.23 eV), reflecting that the adsorption strength is significantly enhanced more thermodynamically favorable on Ni_2P (001)-Cu_3P (1-10) due to the heterointerface. Because the HER is the main competitive reaction during electrocatalytic NO_3RR, the HER performance was also calculated. As presented, the huge H_2 formation energy barrier of Cu_3P-Ni_2P is 2.71 eV, compared with those of Cu_3P (0.868 eV) and Ni_2P (0.33 eV), accounting for the suppressing HER performance (Fig. 5(d)) [7, 66]. Moreover, density of states (DOS) is a useful tool to probe the catalyst electronic structures [67]. The DOS for Cu_3P, Ni_2P, and Ni_2P (001)-Cu_3P (1-10) exhibit that all the phosphide exhibit fully occupied states passing through the Fermi level, indicating its metallic nature (Fig. S21 in the ESM) [68]. Meanwhile, the carrier density near the Fermi level of Ni_2P (001)-Cu_3P (1-10) was significantly enhanced as compared with Cu_3P and Ni_2P, which was beneficial for leading to a higher electrical conductivity and accelerating catalytic kinetics. Thus the Ni_2P (001)-Cu_3P (1-10) catalyst is an active electrocatalyst for NO_3RR.

The operando ATR-IRRAS measurements of Cu_3P-Ni_2P/CP-

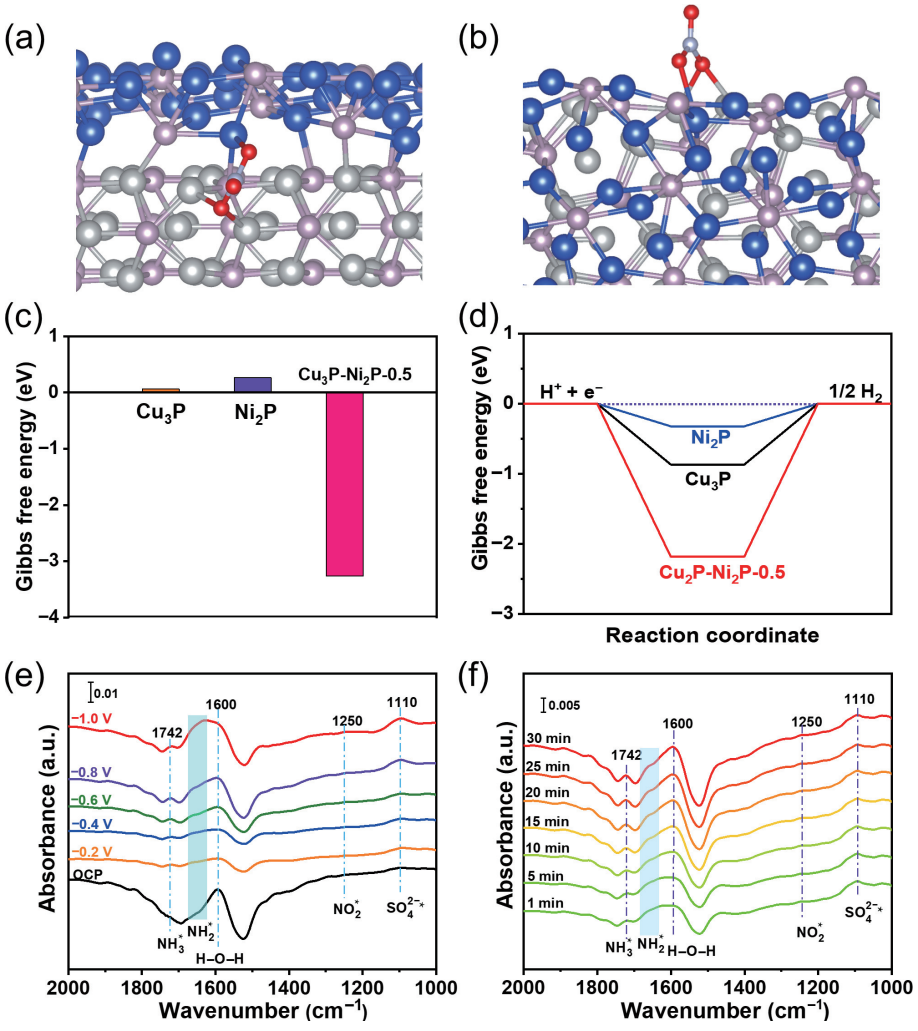

Figure 5 (a) Top view and (b) side view of the optimized NO_3^- adsorption configuration of Cu_3P-Ni_2P-0.5 slab models. (c) Adsorption free energies of NO_3^- on the different catalysts. (d) The calculated ΔG_{H^*} values of HER. Operando ATR-IRRAS spectra of Cu_3P-Ni_2P/CP-0.5 (e) from OCP to −1.0 V (vs. RHE) in electrolytes containing 0.5 M Na_2SO_4 and 200 ppm NO_3^--N, and (f) in an electrolyte containing 0.5 M Na_2SO_4 and 200 ppm NO_3^--N at −0.6 V (vs. RHE) over a 30 min period.

0.5 were carried out to reveal the reaction pathway. The vibration peaks at the same position were observed at different applied voltages (Fig. 5(e)). The positive bands at 1110 and 1250 cm^{-1} are ascribed to SO_4^{2-}* and NO_2^-* [69], demonstrating that the NO_2^- could be an intermediate during electrocatalytic NO_3RR. Additionally, the peak intensity of NH_3* (1742 cm^{-1}) and NH_2* (1640–1670 cm^{-1}) increased significantly with the increase in voltage, reflecting the reaction pathway from NO_3^- to NH_3 (Fig. 5(f)) via successive hydrodeoxygenation [70].

The abovementioned results demonstrated that the Cu_3P-Ni_2P-0.5 could significantly enhance the NO_3^- adsorption and facilitate the formation of ammonia through the successive hydrodeoxygenation pathway of NO_3^-.

4 Conclusions

In summary, heterostructure bimetallic phosphide Cu_3P-Ni_2P/CP-*x* catalysts directly grown on carbon paper were fabricated through a facile vapor-phase hydrothermal method. The optimal Cu_3P-Ni_2P/CP-0.5 exhibited excellent electrocatalytic activities toward the electroreduction of nitrate to ammonia. Moreover, the electrocatalytic NO_3RR performance of Cu_3P-Ni_2P/CP-0.5 was systematically evaluated using three-type electrochemical reactors, including an H-type cell, RDE setup, and MEA electrolyzer. Expectedly, Cu_3P-Ni_2P/CP-0.5 assembled MEA cell with anion exchange membrane exhibited the highest activity toward electrocatalytic NO_3RR to NH_3, delivering the maximum R_{NH3} of 1.9 $mmol \cdot h^{-1} \cdot cm^{-2}$ at the full-cell voltage of 2.6 V (55 °C). The results of *in-situ* spectroscopy characterization combined with theoretical calculations revealed that the adsorption of NO_3* can be effectively regulated by constructing a heterointerface between Cu_3P and Ni_2P, and the reaction mechanism of NO_3^- to NH_3 would follow the successive hydrodeoxygenation pathway. This work would be very significant for the development of high-efficiency transition metal phosphide-based electrocatalysts and novel electrocatalysis systems for electrosynthesis of NH_3.

Acknowledgements

This work was financially supported by the postdoctoral researcher funding project of Anhui Province (No. 2022B585), the HFIPS Director's Fund (No. YZJJ2023QN29), the National Natural Science Foundation of China (No. 52172106), and the Special Research Assistant Program, Chinese Academy of Sciences.

Electronic Supplementary Material: Supplementary material (schematic illustration of fabrication process, TEM image, SEM images, LSV curves, UV–Vis absorption spectra, NO_3RR potentiostatic curves, stability test, constructed theoretical model, and operando ATR-IRRAS experimental setup) is available in the online version of this article at https://doi.org/10.1007/s12274-024-6474-z.

References

[1] Liu, Y. T.; Qiu, W. X.; Wang, P. F.; Li, R.; Liu, K.; Omer, K. M.; Jin, Z. Y.; Li, P. P. Pyridine-N-rich Cu single-atom catalyst boosts nitrate electroreduction to ammonia. *Appl. Catal. B: Environ.* **2024**, *340*, 123228.

[2] Gong, Z. H.; Xiang, X. P.; Zhong, W. Y.; Jia, C. H.; Chen, P. Y.; Zhang, N.; Zhao, S. J.; Liu, W. Z.; Chen, Y.; Lin, Z. Modulating metal-nitrogen coupling in anti-perovskite nitride via cation doping for efficient reduction of nitrate to ammonia. *Angew. Chem., Int. Ed.* **2023**, *135*, e202308775.

[3] Zhang, X. R.; Lyu, Y.; Zhou, H. J.; Zheng, J. Y.; Huang, A. B.; Ding, J. J.; Xie, C.; De Marco, R.; Tsud, N.; Kalinovych, V. et al. Photoelectrochemical N_2-to-NH_3 fixation with high efficiency and rates via optimized Si-based system at positive potential versus $Li^{0/+}$. *Adv. Mater.* **2023**, *35*, 2211894.

[4] Murphy, E.; Liu, Y. C.; Matanovic, I.; Rüscher, M.; Huang, Y.; Ly, A.; Guo, S. Y.; Zang, W. J.; Yan, X. X.; Martini, A. et al. Elucidating electrochemical nitrate and nitrite reduction over atomically-dispersed transition metal sites. *Nat. Commun.* **2023**, *14*, 4554.

[5] Jiang, H. F.; Chen, G. F.; Savateev, O.; Xue, J.; Ding, L. X.; Liang, Z. X.; Antonietti, M.; Wang, H. H. Enabled efficient ammonia synthesis and energy supply in a zinc-nitrate battery system by separating nitrate reduction process into two stages. *Angew. Chem., Int. Ed.* **2023**, *62*, e202218717.

[6] Yuan, J.; Feng, W. H.; Zhang, Y. F.; Xiao, J. Y.; Zhang, X. Y.; Wu, Y. T.; Ni, W. K.; Huang, H. W.; Dai, W. X. Unraveling synergistic effect of defects and piezoelectric field in breakthrough piezo-photocatalytic N_2 reduction. *Adv. Mater.*, in press, DOI: 10.1002/adma.202303845.

[7] Wang, Y. T.; Zhou, W.; Jia, R. R.; Yu, Y. F.; Zhang, B. Unveiling the activity origin of a copper-based electrocatalyst for selective nitrate reduction to ammonia. *Angew. Chem., Int. Ed.* **2020**, *59*, 5350–5354.

[8] Zhao, R. D.; Yan, Q. Y.; Yu, L. H.; Yan, T.; Zhu, X. Y.; Zhao, Z. Y.; Liu, L.; Xi, J. Y. A Bi-Co corridor construction effectively improving the selectivity of electrocatalytic nitrate reduction toward ammonia by nearly 100%. *Adv. Mater.* **2023**, *35*, 2306633.

[9] Hu, Q.; Qin, Y. J.; Wang, X. D.; Wang, Z. Y.; Huang, X. W.; Zheng, H. J.; Gao, K. R.; Yang, H. P.; Zhang, P. X.; Shao, M. H. et al. Reaction intermediate-mediated electrocatalyst synthesis favors specified facet and defect exposure for efficient nitrate-ammonia conversion. *Energy Environ. Sci.* **2021**, *14*, 4989–4997.

[10] Chen, W. D.; Yang, X. Y.; Chen, Z. D.; Ou, Z. J.; Hu, J. T.; Xu, Y.; Li, Y. L.; Ren, X. Z.; Ye, S. H.; Qiu, J. S. et al. Emerging applications, developments, prospects, and challenges of electrochemical nitrate-to-ammonia conversion. *Adv. Funct. Mater.* **2023**, *33*, 2300512.

[11] Gu, Z. X.; Zhang, Y. C.; Wei, X. L.; Duan, Z. Y.; Gong, Q. Y.; Luo, K. Intermediates regulation via electron-deficient Cu sites for selective nitrate-to-ammonia electroreduction. *Adv. Mater.* **2023**, *35*, 2303107.

[12] Yao, F. B.; Jia, M. C.; Yang, Q.; Chen, F.; Zhong, Y.; Chen, S. J.; He, L.; Pi, Z. J.; Hou, K. J.; Wang, D. B. et al. Highly selective electrochemical nitrate reduction using copper phosphide self-supported copper foam electrode: Performance, mechanism, and application. *Water Res.* **2021**, *193*, 116881.

[13] Wang, Y. T.; Wang, C. H.; Li, M. Y.; Yu, Y. F.; Zhang, B. Nitrate electroreduction: Mechanism insight, *in situ* characterization, performance evaluation, and challenges. *Chem. Soc. Rev.* **2021**, *50*, 6720–6733.

[14] Xue, Z. H.; Shen, H. C.; Chen, P. C.; Pan, G. X.; Zhang, W. W.; Zhang, W. M.; Zhang, S. N.; Li, X. H.; Yavuz, C. T. Boronization of nickel foam for sustainable electrochemical reduction of nitrate to ammonia. *ACS Energy Lett.* **2023**, *8*, 3843–3851.

[15] Ren, Z. H.; Shi, K. G.; Feng, X. F. Elucidating the intrinsic activity and selectivity of Cu for nitrate electroreduction. *ACS Energy Lett.* **2023**, *8*, 3658–3665.

[16] Lv, C. D.; Liu, J. W.; Lee, C.; Zhu, Q.; Xu, J. W.; Pan, H. G.; Xue, C.; Yan, Q. Y. Emerging p-block-element-based electrocatalysts for sustainable nitrogen conversion. *ACS Nano* **2022**, *16*, 15512–15527.

[17] Wang, J.; Feng, T.; Chen, J. X.; Ramalingam, V.; Li, Z. X.; Kabtamu, D. M.; He, J. H.; Fang, X. S. Electrocatalytic nitrate/nitrite reduction to ammonia synthesis using metal nanocatalysts and bio-inspired metalloenzymes. *Nano Energy* **2021**, *86*, 106088.

[18] Wang, J.; Feng, T.; Chen, J. X.; He, J. H.; Fang, X. S. Flexible 2D Cu metal: Organic framework@mxene film electrode with excellent durability for highly selective electrocatalytic NH_3 synthesis. *Research* **2022**, *2022*, 9837012.

[19] Sun, W. J.; Ji, H. Q.; Li, L. X.; Zhang, H. Y.; Wang, Z. K.; He, J. H.; Lu, J. M. Built-in electric field triggered interfacial accumulation effect for efficient nitrate removal at ultra-low concentration and electroreduction to ammonia. *Angew. Chem., Int. Ed.* **2021**, *60*, 22933–22939.

[20] Bu, Y. G.; Wang, C.; Zhang, W. K.; Yang, X. H.; Ding, J.; Gao, G. D. Electrical pulse-driven periodic self-repair of Cu-Ni tandem catalyst for efficient ammonia synthesis from nitrate. *Angew. Chem., Int. Ed.* **2023**, *62*, e202217337.
[21] Xu, L. H.; Liu, W. P.; Liu, K. Single atom environmental catalysis: Influence of supports and coordination environments. *Adv. Funct. Mater.* **2023**, *33*, 2304468.
[22] Wang, S. W.; Song, C. F.; Cai, Y. J.; Li, Y. F.; Jiang, P. K.; Li, H.; Yu, B.; Ma, T. Y. Interfacial polarization triggered by covalent-bonded MXene and black phosphorus for enhanced electrochemical nitrate to ammonia conversion. *Adv. Energy Mater.* **2023**, *13*, 2301136.
[23] Zhang, G. K.; Wang, F. Z.; Chen, K.; Kang, J. L.; Chu, K. Atomically dispersed Sn confined in FeS_2 for nitrate-to-ammonia electroreduction. *Adv. Funct. Mater.* **2024**, *34*, 2305372.
[24] Zhou, Y. Y.; Duan, R. Z.; Li, H.; Zhao, M.; Ding, C. M.; Li, C. Boosting electrocatalytic nitrate reduction to ammonia via promoting water dissociation. *ACS Catal.* **2023**, *13*, 10846–10854.
[25] Zhao, G. Q.; Jiang, Y. Z.; Dou, S. X.; Sun, W. P.; Pan, H. G. Interface engineering of heterostructured electrocatalysts towards efficient alkaline hydrogen electrocatalysis. *Sci. Bull.* **2021**, *66*, 85–96.
[26] Tan, Z. X.; Du, F.; Tong, M. Q.; Hu, J. D.; Zhang, N.; Huang, S. Y.; Guo, C. X. Heterostructured CoS_2/MoS_2 with a rich active site for an efficient electrochemical nitrate reduction reaction to ammonia. *Energy Fuels* **2023**, *37*, 18085–18092.
[27] Zhao, X. E.; Li, Z. R.; Gao, S.; Sun, X. P.; Zhu, S. Y. CoS_2@TiO_2 nanoarray: A heterostructured electrocatalyst for high-efficiency nitrate reduction to ammonia. *Chem. Commun.* **2022**, *58*, 12995–12998.
[28] Liu, Y.; Yao, X. M.; Liu, X.; Liu, Z. L.; Wang, Y. Q. $Cu_{2+1}O$/Ag heterostructure for boosting the electrocatalytic nitrate reduction to ammonia performance. *Inorg. Chem.* **2023**, *62*, 7525–7532.
[29] Paul, S.; Sarkar, S.; Adalder, A.; Kapse, S.; Thapa, R.; Ghorai, U. K. Strengthening the metal center of Co–N_4 active sites in a 1D-2D heterostructure for nitrate and nitrogen reduction reaction to ammonia. *ACS Sustainable Chem. Eng.* **2023**, *11*, 6191–6200.
[30] Zheng, L. X.; Ye, W. Q.; Zhao, Y. J.; Lv, Z. Q.; Shi, X. W.; Wu, Q.; Fang, X. S.; Zheng, H. J. Defect-induced atomic arrangement in CoFe bimetallic heterostructures with boosted oxygen evolution activity. *Small* **2023**, *19*, 2205092.
[31] Zhou, P.; Tao, L.; Tao, S. S.; Li, Y. C.; Wang, D. D.; Dong, X. W.; Frauenheim, T.; Fu, X. Z.; Lv, X. S.; Wang, S. Y. Construction of nickel-based dual heterointerfaces towards accelerated alkaline hydrogen evolution via boosting multi-step elementary reaction. *Adv. Funct. Mater.* **2021**, *31*, 2104827.
[32] Liu, D.; Xu, G. Y.; Yang, H.; Wang, H. T.; Xia, B. Y. Rational design of transition metal phosphide-based electrocatalysts for hydrogen evolution. *Adv. Funct. Mater.* **2023**, *33*, 2208358.
[33] Huang, C. J.; Xu, H. M.; Shuai, T. Y.; Zhan, Q. N.; Zhang, Z. J.; Li, G. R. A review of modulation strategies for improving catalytic performance of transition metal phosphides for oxygen evolution reaction. *Appl. Catal. B Environ.* **2023**, *325*, 122313.
[34] Zeng, L. Y.; Sun, K. A.; Wang, X. B.; Liu, Y. Q.; Pan, Y.; Liu, Z.; Cao, D. W.; Song, Y.; Liu, S. H.; Liu, C. G. Three-dimensional-networked Ni_2P/Ni_3S_2 heteronanoflake arrays for highly enhanced electrochemical overall-water-splitting activity. *Nano Energy* **2018**, *51*, 26–36.
[35] Liu, Y. Q.; Zhang, Z. H.; Zhang, L.; Xia, Y. G.; Wang, H. Q.; Liu, H.; Ge, S. G.; Yu, J. H. Manipulating the d-band centers of transition metal phosphides through dual metal doping towards robust overall water splitting. *J. Mater. Chem. A* **2022**, *10*, 22125–22134.
[36] Ren, T. L.; Yu, Z.; Yu, H. J.; Deng, K.; Wang, Z. Q.; Li, X. N.; Wang, H. J.; Wang, L.; Xu, Y. Interfacial polarization in metal–organic framework reconstructed Cu/Pd/CuO_x multi-phase heterostructures for electrocatalytic nitrate reduction to ammonia. *Appl. Catal. B Environ.* **2022**, *318*, 121805.
[37] Ji, X. Y.; Sun, K.; Liu, Z. K.; Liu, X. H.; Dong, W. K.; Zuo, X. T.; Shao, R. W.; Tao, J. Identification of dynamic active sites among Cu species derived from MOFs@CuPc for electrocatalytic nitrate reduction reaction to ammonia. *NanoMicro Lett.* **2023**, *15*, 110.
[38] Xu, Z. A.; Wan, L.; Liao, Y. W.; Pang, M. B.; Xu, Q.; Wang, P. C.; Wang, B. G. Continuous ammonia electrosynthesis using physically interlocked bipolar membrane at 1000 $mA \cdot cm^{-2}$. *Nat. Commun.* **2023**, *14*, 1619.
[39] Zhang, X.; Han, M. M.; Liu, G. Q.; Wang, G. Z.; Zhang, Y. X.; Zhang, H. M.; Zhao, H. J. Simultaneously high-rate furfural hydrogenation and oxidation upgrading on nanostructured transition metal phosphides through electrocatalytic conversion at ambient conditions. *Appl. Catal. B Environ.* **2019**, *244*, 899–908.
[40] Jin, M.; Zhang, X.; Han, M. M.; Wang, H. J.; Wang, G. Z.; Zhang, H. M. Efficient electrochemical N_2 fixation by doped-oxygen-induced phosphorus vacancy defects on copper phosphide nanosheets. *J. Mater. Chem. A* **2020**, *8*, 5936–5942.
[41] Wouters, B.; Sheng, X.; Boschin, A.; Breugelmans, T.; Ahlberg, E.; Vankelecom, I. F. J.; Pescarmona, P. P.; Hubin, A. The electrocatalytic behaviour of Pt and Cu nanoparticles supported on carbon nanotubes for the nitrobenzene reduction in ethanol. *Electrochim. Acta* **2013**, *111*, 405–410.
[42] Daems, N.; Wouters, J.; Van Goethem, C.; Baert, K.; Poleunis, C.; Delcorte, A.; Hubin, A.; Vankelecom, I. F. J.; Pescarmona, P. P. Selective reduction of nitrobenzene to aniline over electrocatalysts based on nitrogen-doped carbons containing non-noble metals. *Appl. Catal. B Environ.* **2018**, *226*, 509–522.
[43] Wang, C. H.; Liu, Z. Y.; Hu, T.; Li, J. S.; Dong, L. Q.; Du, F.; Li, C. M.; Guo, C. X. Metasequoia-like nanocrystal of iron-doped copper for efficient electrocatalytic nitrate reduction into ammonia in neutral media. *ChemSusChem* **2021**, *14*, 1825–1829.
[44] Kresse, G.; Hafner, J. *Ab initio* molecular-dynamics simulation of the liquid-metal-amorphous-semiconductor transition in germanium. *Phys. Rev. B* **1994**, *49*, 14251–14269.
[45] Perdew, J. P.; Burke, K.; Ernzerhof, M. Generalized gradient approximation made simple. *Phys. Rev. Lett.* **1996**, *77*, 3865–3868.
[46] Grimme, S. Semiempirical GGA-type density functional constructed with a long-range dispersion correction. *J. Comput. Chem.* **2006**, *27*, 1787–1799.
[47] Grimme, S.; Antony, J.; Ehrlich, S.; Krieg, H. A consistent and accurate *ab initio* parametrization of density functional dispersion correction (DFT-D) for the 94 elements H-Pu. *J. Chem. Phys.* **2010**, *132*, 154104.
[48] Wang, V.; Xu, N.; Liu, J. C.; Tang, G.; Geng, W. T. VASPKIT: A user-friendly interface facilitating high-throughput computing and analysis using VASP code. *Comput. Phys. Commun.* **2021**, *267*, 108033.
[49] Huang, Y. M.; Yang, R.; Wang, C. H.; Meng, N. N.; Shi, Y. M.; Yu, Y. F.; Zhang, B. Direct electrosynthesis of urea from carbon dioxide and nitric oxide. *ACS Energy Lett.* **2022**, *7*, 284–291.
[50] Wu, L. B.; Yu, L.; Zhang, F. H.; McElhenny, B.; Luo, D.; Karim, A.; Chen, S.; Ren, Z. F. Heterogeneous bimetallic phosphide Ni_2P-Fe_2P as an efficient bifunctional catalyst for water/seawater splitting. *Adv. Funct. Mater.* **2021**, *31*, 2006484.
[51] Liu, C. C.; Gong, T.; Zhang, J.; Zheng, X. R.; Mao, J.; Liu, H.; Li, Y.; Hao, Q. Y. Engineering Ni_2P-$NiSe_2$ heterostructure interface for highly efficient alkaline hydrogen evolution. *Appl. Catal. B Environ.* **2020**, *262*, 118245.
[52] Chen, J. Y.; Li, X.; Ma, B.; Zhao, X. D.; Chen, Y. T. Cu_3P@Ni core-shell heterostructure with modulated electronic structure for highly efficient hydrogen evolution. *Nano Res.* **2022**, *15*, 2935–2942.
[53] Gang, C.; Chen, J.; Li, X.; Ma, B.; Zhao, X.; Chen, Y. Cu_3P@CoO core–shell heterostructure with synergistic effect for highly efficient hydrogen evolution. *Nanoscale* **2021**, *13*, 19430–19437.
[54] Qin, X. Y.; Yan, B. Y.; Kim, D.; Teng, Z. S.; Chen, T. Y.; Choi, J.; Xu, L.; Piao, Y. Interfacial engineering and hydrophilic/aerophobic tuning of Sn_4P_3/Co_2P heterojunction nanoarrays for high-efficiency fully reversible water electrolysis. *Appl. Catal. B Environ.* **2022**, *304*, 120923.
[55] Yang, B. P.; Zhou, Y. L.; Huang, Z. C.; Mei, B. B.; Kang, Q.; Chen, G.; Liu, X. H.; Jiang, Z.; Liu, M.; Zhang, N. Electron-deficient cobalt nanocrystals for promoted nitrate electrocatalytic reduction to synthesize ammonia. *Nano Energy* **2023**, *117*, 108901.
[56] Guharoy, U.; Reina, T. R.; Olsson, E.; Gu, S.; Cai, Q. Theoretical insights of Ni_2P (0001) surface toward its potential applicability in

CO_2 conversion via dry reforming of methane. *ACS Catal.* **2019**, *9*, 3487–3497.

[57] Jin, M.; Liu, Y. Y.; Zhang, X.; Wang, J. L.; Zhang, S. B.; Wang, G. Z.; Zhang, Y. X.; Yin, H. J.; Zhang, H. M.; Zhao, H. J. Selective electrocatalytic hydrogenation of nitrobenzene over copper-platinum alloying catalysts: Experimental and theoretical studies. *Appl. Catal. B Environ.* **2021**, *298*, 120545.

[58] Yang, Y.; Li, F. W. Reactor design for electrochemical CO_2 conversion toward large-scale applications. *Curr. Opin. Green Sustain. Chem.* **2021**, *27*, 100419.

[59] Gao, D. F.; Wei, P. F.; Li, H. F.; Lin, L.; Wang, G. X.; Bao, X. H. Designing electrolyzers for electrocatalytic CO_2 reduction. *Acta Phys. Chim. Sin.* **2021**, *37*, 2009021.

[60] Lagadec, M. F.; Grimaud, A. Water electrolysers with closed and open electrochemical systems. *Nat. Mater.* **2020**, *19*, 1140–1150.

[61] Weng, L. C.; Bell, A. T.; Weber, A. Z. Towards membrane-electrode assembly systems for CO_2 reduction: A modeling study. *Energy Environ. Sci.* **2019**, *12*, 1950–1968.

[62] Higgins, D.; Hahn, C.; Xiang, C. X.; Jaramillo, T. F.; Weber, A. Z. Gas-diffusion electrodes for carbon dioxide reduction: A new paradigm. *ACS Energy Lett.* **2019**, *4*, 317–324.

[63] Gabardo, C. M.; O'Brien, C. P.; Edwards, J. P.; McCallum, C.; Xu, Y.; Dinh, C. T.; Li, J.; Sargent, E. H.; Sinton, D. Continuous carbon dioxide electroreduction to concentrated multi-carbon products using a membrane electrode assembly. *Joule* **2019**, *3*, 2777–2791.

[64] Kutz, R. B.; Chen, Q. M.; Yang, H. Z.; Sajjad, S. D.; Liu, Z. C.; Masel, I. R. Sustainion imidazolium-functionalized polymers for carbon dioxide electrolysis. *Energy Technol.* **2017**, *5*, 929–936.

[65] Shao, Q.; Wang, P. T.; Huang, X. Q. Opportunities and challenges of interface engineering in bimetallic nanostructure for enhanced electrocatalysis. *Adv. Funct. Mater.* **2019**, *29*, 1806419.

[66] Jia, R. R.; Wang, Y. T.; Wang, C. H.; Ling, Y. F.; Yu, Y. F.; Zhang, B. Boosting selective nitrate electroreduction to ammonium by constructing oxygen vacancies in TiO_2. *ACS Catal.* **2020**, *10*, 3533–3540.

[67] Chen, Z. W.; Chen, L. X.; Wen, Z.; Jiang, Q. Understanding electrocatalysis by using density functional theory. *Phys. Chem. Chem. Phys.* **2019**, *21*, 23782–23802.

[68] Qian, Q. Z.; Zhang, J. H.; Li, J. M.; Li, Y. P.; Jin, X.; Zhu, Y.; Liu, Y.; Li, Z.; El-Harairy, A.; Xiao, C. et al. Artificial heterointerfaces achieve delicate reaction kinetics towards hydrogen evolution and hydrazine oxidation catalysis. *Angew. Chem., Int. Ed.* **2021**, *60*, 5984–5993.

[69] Wang, Y. L.; Yin, H. B.; Dong, F.; Zhao, X. G.; Qu, Y. K.; Wang, L. X.; Peng, Y.; Wang, D. S.; Fang, W.; Li, J. H. N-coordinated Cu-Ni dual-single-atom catalyst for highly selective electrocatalytic reduction of nitrate to ammonia. *Small* **2023**, *19*, 2207695.

[70] Zhou, N.; Wang, Z.; Zhang, N.; Bao, D.; Zhong, H. X.; Zhang, X. B. Potential-induced synthesis and structural identification of oxide-derived Cu electrocatalysts for selective nitrate reduction to ammonia. *ACS Catal.* **2023**, *13*, 7529–7537.